Semi-Transparent Polymer Solar Cells with Excellent Sub-Bandgap Transmission for Third Generation Photovoltaics

*Zach M. Beiley, M. Greyson Christoforo, Paul Gratia, Andrea R. Bowring, Petra Eberspacher, George Y. Margulis, Clément Cabanetos, Pierre M. Beaujuge, Alberto Salleo, and Michael D. McGehee**

Semi-transparent organic photovoltaics (OPV) are of great interest for photovoltaic applications that require a portion of the light to be transmitted through the solar cell. These include aesthetic applications, such as building-integrated photovoltaics and solar windows,[1–3] as well as third generation high efficiency photovoltaic architectures, such as photovoltaics with up-converting absorbers[4,5] and hybrid tandem photovoltaics (HTPV).[6] In HTPV a high bandgap organic cell is placed on top of a more conventional inorganic photovoltaic, such as silicon or $CuIn_xGa_{(1-x)}Se_2$ (CIGS), to form a higher efficiency tandem cell. Previously we modeled the efficiencies of HTPV devices and showed that they have the potential to improve the efficiency of moderately performing (~15%) inorganic cells to over 20%.[6] In all of these applications, the organic cell must be highly efficient while at the same time transmitting the light not absorbed by the organic active layer. Loss of transmission primarily comes from the absorption and reflection of the transparent electrodes and is typically most severe in the red and near-IR. The transmission of these low energy photons, which are lower in energy than the bandgap of most organic absorbers, is particularly important for HTPV and up-converting cells, because it is essential for the bottom cell or up-converter to receive as much light as possible. However sub bandgap transmission is not often studied in semi-transparent cells. Arguably the most challenging part of fabricating a high performing semi-transparent cell is depositing a transparent electrode on top of the organic active layer. The requirements for this layer are stringent; it must be conducting enough to collect photogenerated carriers with low resistive losses while being as transparent as possible to unabsorbed light. It has been estimated that for a transparent conducting technology to be incorporated into photovoltaic modules it must achieve transmission greater than 90% with a sheet resistance less than 10 Ω sq^{-1}.[7] Furthermore, for this application it must be deposited gently at low temperatures, because organic absorbers can be damaged by high temperature processing,[8] and the UV radiation and ion bombardment of sputter deposition.[9,10] In the past researchers have fabricated semi-transparent OPV devices with good electrical performance using transparent electrodes based on conducting polymers,[11–14] very thin metal films,[2,15] sputtered transparent conducting oxides,[9] carbon nanotubes,[16] graphene[17] and silver nanowires (Ag NWs).[1,18–22] However, these devices have generally had relatively inefficient transmission of light not absorbed by the organic active layer, or else use electrodes that are far from the 10 Ω sq^{-1} benchmark required for making modules. In this Communication, we demonstrate semi-transparent OPV devices using an Ag NW–ZnO nanoparticle (ZnO NP) composite top electrode that have a power conversion efficiency of 5.0%, the highest reported for a semi-transparent cell using Ag NWs. The Ag NW – ZnO NP composite electrode has a sheet resistance of 14 Ω sq^{-1} with a peak transmission of 93.5%, and is solution processed entirely at room temperature. Furthermore, the semi-transparent cells have superior optical performance, transmitting ~81% of the light below and ~34% of the light above the bandgap of the organic absorber. We also discuss our approach to designing these cells, which has relied heavily on transfer matrix optical modeling[23–25] both as a predictive tool to guide our design choices and as a method of characterization.

We have chosen to use a top electrode based on networks of Ag NWs because they are capable of achieving transmission as high as 90% with sheet resistances below 10 Ω sq^{-1}[26] and can be solution processed at low temperature, either beneath or on top of organic active layers.[20,27–29] However, in order for all the photogenerated carriers to be efficiently collected by such an electrode, it has been shown[30] that there must be a material filling the spaces between the Ag NWs that is capable of transporting carriers to the nearest wire with negligible resistive losses. In our Ag NW mesh the distance between nanowires is ~1 μm (Supporting Information, Figure 1), from which we estimate that the filling material must have a sheet resistance less than ~1×10^9 Ω sq^{-1} for the resistive losses due to this lateral transport to be negligible. The conductivity requirements for this filling material are not very stringent – approximately eight orders of magnitude less than the ~10 Ω sq^{-1} that are required

Z. M. Beiley, P. Gratia, A. R. Bowring, P. Eberspacher, Prof. A. Salleo, Prof. M. D. McGehee
Department of Materials Science and Engineering
Stanford University
476 Lomita Mall, Stanford, CA, 94305, USA
E-mail: mmcgehee@stanford.edu
M. G. Christoforo
Department of Electrical Engineering
Stanford University
Stanford, CA, 94305, USA
G. Y. Margulis
Department of Applied Physics
Stanford University
Stanford, CA, 94305, USA
Dr. C. Cabanetos, Prof. P. M. Beaujuge
King Abdullah University of Science and Technology (KAUST)
Thuwal, 23955–6900, Saudi Arabia

DOI: 10.1002/adma.201301985

for the electrode on a macroscopic scale (i.e. the Ag NWs themselves). Nevertheless, some filling material is necessary because the organic active layer is typically three orders of magnitude too resistive to accomplish the lateral transport on its own (see Supporting Information for details). Researchers have previously used conductive polymers,[1,18,22,31,32] indium tin oxide (ITO) nanoparticles,[21,30] and intrinsic[33,34] and doped[35,36] ZnO nanoparticles to fill Ag NW meshes. We use intrinsic ZnO nanoparticles that have an enhanced conductivity[34] because of an off-stoichiometry Pacholski[37] synthesis. We measured the conductivity of these ZnO NPs by taking current-voltage measurements of high aspect ratio two-terminal devices with different geometries. With only very brief exposure to 1 sun AM1.5 G light, such as would be experienced in a solar cell current-voltage test, their conductivity is $2.8 \pm 0.3 \times 10^{-4}$ S cm^{-1}. Because of the photoconductivity of ZnO,[38] after ~2 minutes of light soaking the conductivity rises ~18× to $4.9 \pm 1.9 \times 10^{-3}$ S cm^{-1}. The thickness of ZnO NPs we use in our composite electrode is ~75 nm, giving a sheet resistance of 3–48 $\times 10^{7}$ Ω sq^{-1}, depending on the amount of time they are exposed to light. This sheet resistance is more than sufficient to meet the ~1×10^{9} Ω sq^{-1} requirement to fill the Ag NW mesh without resistive losses, but the carrier density is still low enough to avoid significant optical absorption. Previous efforts[21] to fill the gaps in Ag NW meshes have used ITO NPs whose sheet resistance is ~1×10^{5} Ω sq^{-1}. We have also made devices using ITO NPs to fill the Ag NW mesh and find that using a higher conductivity filler does not improve solar cell performance over using ZnO NPs. We prefer ZnO NPs because the high carrier density of ITO NPs causes more parasitic optical absorption in both the visible and near-IR (Supporting Information: Table 1 and Figure 2).

By combining ZnO NPs with Ag NWs the electrode functions as a composite, with short range (~1 μm) carrier transport occurring in the ZnO NPs and long range (~1 cm) carrier transport occurring in the Ag NW network. As can be seen in **Figure 1**b, the ZnO NPs make excellent conformal contact to the Ag NWs. We find that embedding the Ag NWs in ZnO NPs somewhat improves the sheet resistance of the meshes, reducing it, for example, from 16 Ω sq^{-1} to 14 Ω sq^{-1} in the case of a denser Ag NW mesh and from 80 Ω sq^{-1} to 63 Ω sq^{-1} in the case of a sparser Ag NW mesh. This finding is consistent with previous reports of improving the conductivity of Ag NW electrodes by the addition of a mesh filling material.[33,39,40] The nanoparticles also serve to planarize the top surface of the composite, which is important for the deposition of any subsequent layers, in this case an anti-reflective LiF layer. Figure 1c shows the transmission of composite electrodes with Ag NW meshes of two different densities. The transmission of the composite electrode itself was obtained by measuring total (specular plus diffuse) transmission through the composite on a glass substrate and subtracting the transmission losses of the bare glass. The 14 Ω sq^{-1} composite, which we use on top of the semi-transparent cells, has a peak transmission of 93.5% at 700 nm, and an average transmission (350–1100 nm) of 90.2%. A less dense Ag NW mesh has a sheet resistance of 63 Ω sq^{-1} and can reach a peak transmission of 97.5% (750 nm), with an average transmission of 95.4%. These figures of merit are in line with the best reports for Ag NW electrodes,[40] though our procedure does not include any annealing or mechanical pressing[28] of the Ag NWs.

We have optimized the structure of our semi-transparent cell (Figure 1a), including choice of layers and their thicknesses, for both power conversion efficiency and minimization of optical losses. In our optical modeling we chose the efficiency of a hybrid tandem photovoltaic as the goal of our optimization because HTPV efficiency balances absorption in the organic active layer, which determines the semi-transparent cell efficiency, with transmission of unabsorbed light (400–1000 nm), which determines the efficiency of the inorganic cell beneath it (Supporting Information, Figure 3). In addition to transfer matrix modeling, we fabricated semi-transparent cells with a range of thicknesses of each layer in the cell in order to assess electrical performance and to confirm the validity of our optical modeling. We obtained the best performance with the following architecture. We use 5 nm of MoO_x as the hole collecting electrode, because it yields excellent electrical performance with a variety of bulk heterojunction active layers[41,42] and transfer matrix modeling shows that it results in less reflection and parasitic absorption compared to cells that use the conducting polymer PEDOT: PSS. The active layer of our semi-transparent cell is a bulk heterojunction (120 nm thick) composed of poly(di(2-ethylhexyloxy)benzo[1,2-*b*:4,5-*b*′]dithiophene-*co*-octylthieno[3,4-*c*]pyrrole-4,6-dione) (PBDTTPD) and $PC_{70}BM$ in a 1:1.5 ratio (by weight). This active layer reaches efficiencies up to 8.5% in our lab and in the literature with a reflective Ca/ Al

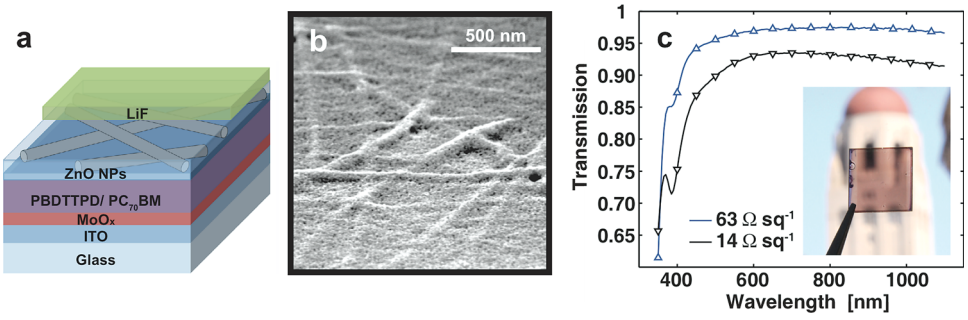

Figure 1. a) Schematic of the semi-transparent cell architecture. The LiF layer is partially removed in the schematic to better show the underlying layers, but covers the entire cell active area in actual devices. b) SEM image of Ag NWs embedded in ZnO NPs forming a 14 Ω sq^{-1} composite electrode. c) Transmission of Ag NW – ZnO NP composite electrodes with different sheet resistances. The reflection and absorption of the glass substrate has been subtracted. The inset shows a photograph of a semi-transparent cell.

top electrode,[43] which allows light multiple passes through the active layer. ZnO NPs function as the electron collecting contact, as well as the conductive filler material of the Ag NW composite. Transfer matrix modeling shows that using a ZnO NP layer with thickness between 50–75 nm minimizes the reflection from the cell. The top-most layer in our architecture is 90 nm of LiF, which is electronically inactive in the cell, and serves as an anti-reflection coating. The LiF primarily reduces reflection in the red and near-IR (620–1100 nm); for example, when light is incident on the Ag NWs side of the device, we estimate using transfer matrix modeling that it increases transmission from 67% to 75% at 1000 nm and from 77% to 84% at 800 nm.

Using our optimization method, we were able to fabricate semi-transparent cells with efficiencies up to 5.0% (**Figure 2**, **Table 1**). Table 1 shows that the fill factor (*FF*) of the semi-transparent cell (0.60) is very close to that of an opaque control device with evaporated silver (0.61). This indicates that the resistive losses in the Ag NW – ZnO NP composite electrode are small and that it is efficient at carrying current over both short and long length scales (the device active area is 0.415 cm^2). The primary difference in performance between the semi-transparent cell and the opaque device is the short-circuit current density (J_{sc}); the semi-transparent cell has a significantly lower J_{sc}, because without a reflective back electrode, the light only has a single pass through the active layer, resulting in lower absorption. Table 1 also shows that the semi-transparent cell is significantly better when illuminated from the glass side of the device (5.0%) compared to when it is illuminated from the Ag NWs side (4.3%). The main difference is in J_{sc}, but the *FF* and open circuit voltage (V_{oc}) are also slightly higher for the cell when it is illuminated from the glass side. In order to determine whether these differences are due to better transmission of light through the glass than the Ag NWs, or to difference in charge collection efficiency, we measured[23] the internal quantum efficiency (IQE) of the cell when illuminated from both sides of the device (Figure 2). When illuminated from the Ag NWs side of the device, the average IQE (400–630 nm) is 78%, while when illuminated from the glass side of the device it is 87%. This demonstrates that the device is more efficient when illuminated from the glass side of the device because photogenerated carriers are collected more efficiently, not because more light reaches the active layer. Not only does this account for the difference in J_{sc}, it also helps to explain the differences in *FF* and V_{oc}. When the device is illuminated from the glass side more light is absorbed in the active layer close to the MoO_x, which is the hole-collecting electrode. By contrast, when the device is illuminated from the Ag NWs side more light is absorbed in the active layer near the ZnO NPs, which is the electron-collecting electrode. Holes are known to be the slower of the two charge carriers in PBDTTPD/ PCBM blends,[8] so photogenerated carriers are collected more efficiently when they are generated closer to the hole-collecting electrode.[44] This is particularly important when the electric field in the active layer is low (i.e. at the maximum power point and V_{oc}), which accounts for the higher observed V_{oc} and *FF*.

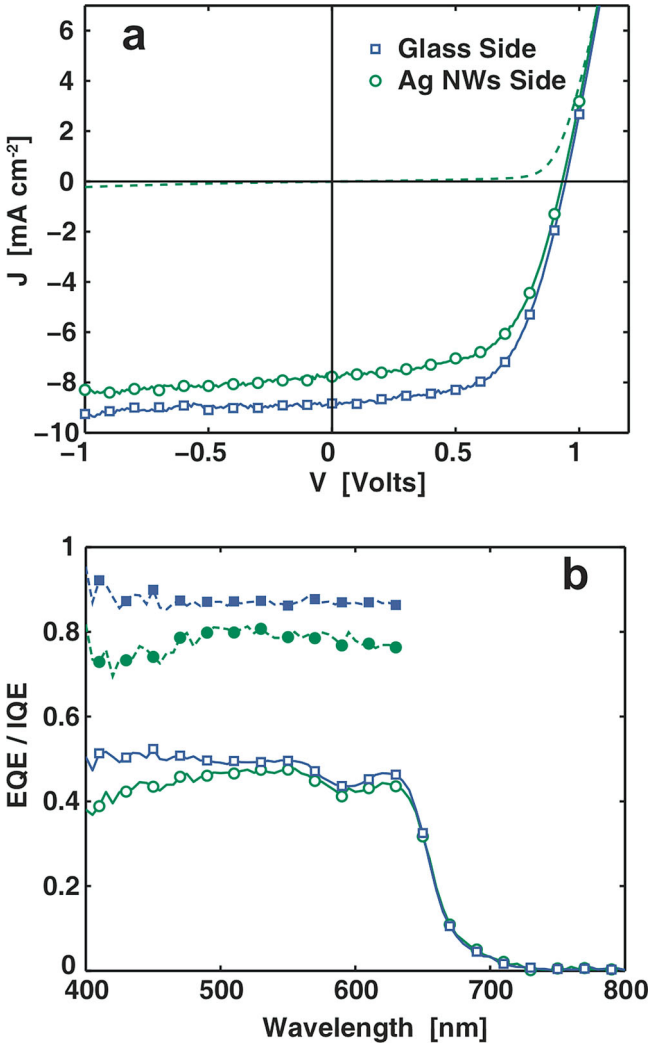

Figure 2. a) Current-voltage characteristics of the 5.0% semi-transparent cell when illuminated from the glass and Ag NWs sides of the device. The dashed line shows the current in the dark. b) External (open symbols) and internal (filled symbols) quantum efficiencies for the same cell when illuminated from the glass and Ag NWs sides of the device. The EQE-integrated J_{sc} is 8.6 mA cm^{-2} and 7.8 mA cm^{-2} for glass side and Ag NWs side illumination, respectively, which deviate by < 2% from the J_{sc} as determined from the current-voltage characteristics.

Table 1. Efficiency and figures of merit for the best semi-transparent solar cell using a 14 Ω sq^{-1} Ag NW composite electrode when illuminated from the glass and Ag NWs sides of the device. For comparison, the figures of merit for opaque control devices with evaporated Ag and Ca/Al are included.

	Glass Side	Ag NWs Side	Evaporated Ag	Evaporated Ca/ Al
Efficiency	5.03%	4.30%	6.59%	8.54%
J_{sc} [mA·cm^{-2}]	8.83	7.77	11.8	12.9
V_{oc} [V]	0.945	0.931	0.918	0.950
FF	0.60	0.59	0.61	0.69
R_s [Ω·cm^2]	14.7	14.8	2.5	1 .3
Active Layer Thickness [nm]	120	120	120	100

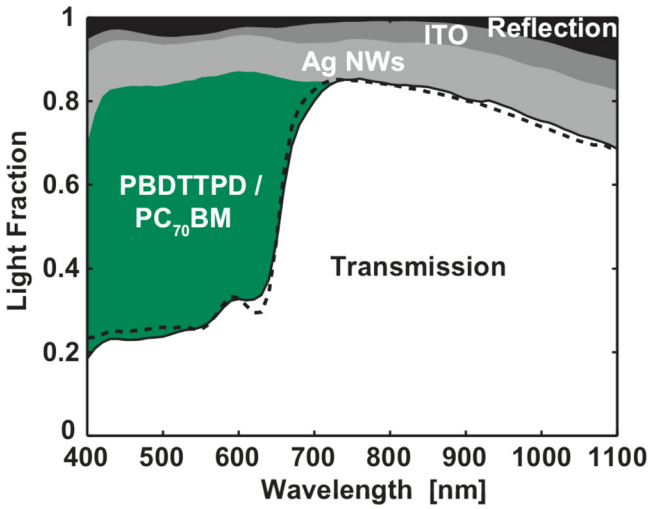

Figure 3. Experimentally measured (dashed black line) and modeled (solid black line) transmission of the 5.0% semi-transparent cell and the components accounting for the optical losses (colored areas) as determined by transfer matrix modeling.

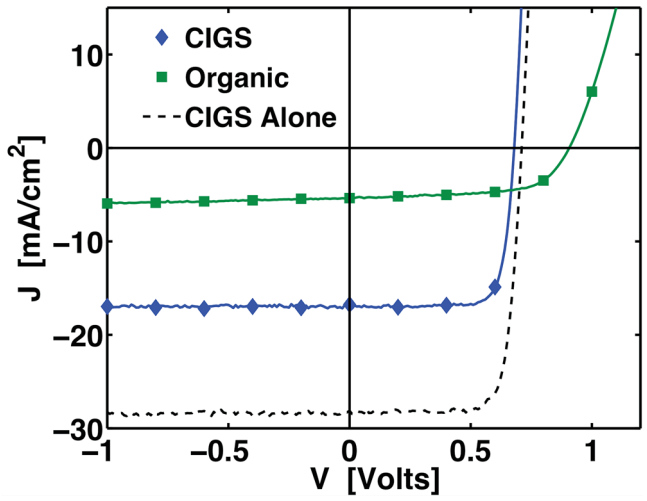

Figure 4. Measured current-voltage curves of the subcells of a mechanically stacked hybrid tandem device. The semi-transparent organic top cell uses ITO NPs instead of ZnO NPs to fill the Ag NW mesh, and is illuminated from the Ag NWs side of the device, so is only 3.1% instead of 5.0%. The measured characteristics of the CIGS cell by itself are also shown (dashed line).

Figure 3 shows the total (specular plus diffuse) transmission of the semi-transparent solar cell as well as the contributions to the optical losses, which we estimate from transfer matrix modeling. The dashed line shows the experimentally measured transmission of the cell when illuminated through the Ag NWs side of the device, which is a maximum at 85% (730 nm) and has an average sub bandgap (700–1000 nm) transmission of 81% and an average above bandgap transmission (400–700 nm) of 34%. The solid line shows the transmission as determined by transfer matrix modeling, which has very good correspondence to the experimentally measured transmission. The colored bands represent the optical losses in the cell, as determined by transfer matrix modeling. The band labeled "Ag NWs" represents the total optical losses due to the Ag NWs, including both absorption and reflection, which average 10.5% (400–1000 nm). The band labeled "Reflection" accounts for reflection off all of the layers in the cell except for Ag NWs and is an average ~2% (400–1000 nm). The active layer absorbs ~60% of the above bandgap light. The absorption of the ZnO NPs in the visible and near-IR is negligible (<1%), so it does not appear on the plot. When light is incident on the glass side of the device, the total transmission is identical to when it is incident on the Ag NWs side, though the relative contributions to the optical losses are different (Supporting Information, Figure 4). If a sparser Ag NW mesh is used (63 Ω sq^{-1}), then the maximum transmission reaches 89.6% (730 nm) with an average sub bandgap (700–1000 nm) transmission 86% and an average above bandgap (400–700 nm) transmission of 37%. In this case, the cell efficiency is still 4.8% from the glass side and 4.4% from the Ag NWs side of the device.

Using our semi-transparent OPV devices we fabricated a mechanically stacked 4-terminal hybrid tandem photovoltaic as a proof-of-concept demonstration. We stacked the semi-transparent organic cells on top of a CIGS solar cell separated by a thin, electrically insulating spacer, and measured each subcell's current-voltage characteristics with 1 sun incident first on the semi-transparent organic cell (**Figure 4**). By itself, the efficiency of the CIGS cell was measured to be 15.7%. When a semi-transparent cell using ITO NPs to fill the gaps in the Ag NW mesh was stacked on top of it, the CIGS cell was only 8.6% efficient, because much of the above and some of the below bandgap light was absorbed by the organic top cell. In this configuration the hybrid tandem is a 4-terminal device, so there are no current or voltage matching constraints and the power output of the two subcells may be added together to get the efficiency of the hybrid tandem itself. Adding the maximum power output of this semi-transparent organic cell to that of the CIGS cell when stacked underneath it gives a measured hybrid tandem efficiency of 11.7% (**Table 2**).

We use measurements on this proof-of-concept device to demonstrate that we can predict the performance of mechanically stacked hybrid tandems by calculating their efficiency. From transmission measurements of the semi-transparent cells and the external quantum efficiency spectrum of the CIGS bottom cell (Supporting Information, Figure 5), we calculated the J_{sc} of the CIGS cell when it is illuminated by light that is first passed through the semi-transparent organic cell. This combined with the current-voltage characteristics of the semi-transparent cell allows us to calculate the efficiency of the mechanically stacked hybrid tandem. Using the above semi-transparent cell with ITO NPs filling the gaps in the Ag NW mesh (3.1% efficiency), we calculate that the mechanically stacked hybrid tandem should have an efficiency of 11.6%. This is in excellent agreement with what we measured in our proof-of-concept demonstration (11.7% efficiency), and gives us confidence that calculations of hybrid tandem efficiencies can accurately predict the performance of actual devices in this configuration. Using the same method, we also calculated the efficiency of a hypothetical hybrid tandem photovoltaic where the top cell is our best performing semi-transparent cell, which uses ZnO NPs to fill the gaps in the Ag NWs and has

Table 2. Efficiency and figures of merit of mechanically stacked hybrid tandem devices using semi-transparent organic top cells with either ITO NPs or ZnO NPs. For the device with ITO NPs, the mechanically stacked hybrid tandem was fabricated and the figures of merit were experimentally measured with light incident on the Ag NWs side of the organic top cell. For the device with ZnO NPs, the hybrid tandem efficiency was calculated from the measured transmission of the semi-transparent organic cell. The measured characteristics of the CIGS cell by itself are also shown.

	CIGS Alone	CIGS Under Organic with ITO NPs	Organic with ITO NPs	CIGS Under Organic with ZnO NPs	Organic with ZnO NPs
Efficiency	15.7%	8.6%	3.1%	9.5%	5.0%
J_{sc} [mA·cm^{-2}]	28.1	16.0	5.36	17.6	8.80
V_{oc} [V]	0.710	0.685	0.906	0.685	0.945
FF	0.79	0.79	0.64	0.79	0.60
HTPV Efficiency		11.7%		14.5%	

an efficiency of 5.0% (Supporting Information, Figure 5). Assuming the bottom cell is the same 15.7% efficient CIGS cell, we estimate that the resulting hybrid tandem would have an efficiency of 14.5% (Table 2). This is significantly better than the HTPV device using a top cell with ITO NPs, because the cell with ZnO NPs is both more efficient and more transparent to sub bandgap light, but is still 1.2 percentage points worse than the CIGS cell by itself.

The main reason that this semi-transparent cell is not capable of improving the 15.7% CIGS cell is that the organic cell cannot be made thick enough to absorb all of the above bandgap light without loss of *FF* and *IQE*. It is known that for this and many other polymer systems there is a significant drop in fill factor when the active layer thickness exceeds ~100 nm, producing a trade-off between fill factor and light absorption or J_{sc}.[8,45] The active layer thickness that we found to be optimal for the semi-transparent cells, 120 nm, is thicker than the optimal active layer thickness of an opaque cell using the polymer PBDTTPD (typically ~100 nm). The best opaque cells (using a Ca/ Al top contact) using this polymer can achieve a *FF* exceeding 0.70.[43] We estimate with transfer matrix modeling that in order to make an HTPV device with a PBDTTPD based semi-transparent cell that matches the efficiency of a 15.7% CIGS cell, the semi-transparent top cell would need to maintain a *FF* of 0.70 and an *IQE* of 90% with an active layer thickness of 150 nm (~67% absorption in a single pass of light through the active layer). Alternatively, a semi-transparent OPV with the *FF*, *IQE*, active layer absorption and transmission of the current cell could make an HTPV device that ties the efficiency of a 15.7% CIGS cell if it achieved a V_{oc} of 1.17 V, instead of 0.945 V. This corresponds to a V_{oc} that is ~0.6 V less than the polymer bandgap (~1.8 eV) divided by the electron charge, which is an empirical scaling often found for the highest voltage organic photovoltaics.[46] We expect that in the next few years it will be possible to increase the thickness and voltage of organic solar cells to meet these targets.

We have developed a semi-transparent OPV architecture that uses an Ag NW – ZnO NP composite as the top electrode and allows the cell to achieve high efficiencies with minimal optical losses. The Ag NW – ZnO NP composite top electrode has a low sheet resistance of 14 Ω sq^{-1}, which approaches what will be required for large scale module manufacturing, and is solution processed at room temperature, making it compatible with low cost, high throughput fabrication techniques. These advances will be instrumental in the development of HTPV devices with efficiencies exceeding 20%, because HTPV requires that a transparent electrode be deposited on top of the organic active layer in both 4-terminal and 2-terminal architectures.[47,48] Although at present it is not possible improve the efficiency of a 15.7% efficient CIGS cell by adding our 5.0% efficient semi-transparent cell on top of it, our semi-transparent cell architecture paves the way for HTPV technology. Advances in the understanding of organic photovoltaics will lead to polymer blends that achieve higher open circuit voltages and can be made thick enough to absorb all of the above bandgap light without loss of *FF*. Our semi-transparent device architecture may also aid other applications where a transparent electrode is deposited on top of an organic active layer, such as organic-organic tandem photovoltaics[13,49] and OPVs built on opaque substrates[27,50,51] such as metal foils. We believe that this technology will speed the development of high efficiency organic photovoltaics in applications ranging from solar windows to hybrid tandems with efficiencies exceeding 20%.

Experimental Section

Semi-transparent cell fabrication (in brief): MoO_x (5 nm) was deposited by thermal evaporation on cleaned and patterned 15 Ω sq^{-1} ITO coated glass substrates. The active layer was a 1:1.5 by weight blend of PBDTTPD/ $PC_{70}BM$, and was deposited by spin coating resulting in a layer thickness of 120 nm. The fabrication of the Ag NW – ZnO NP composite electrode was accomplished in three separate steps. First, a single layer of ZnO NPs was deposited by spin coating from methanol on top of the dry active layer, resulting in a film with a thickness of ~25 nm. Synthesis of the ZnO NPs was adapted from[34] and is described in detail in the Supporting Information. The opaque control devices were completed by depositing silver contacts with an area of 0.1 cm^2. Opaque devices with Ca/ Al top contacts used ~30 nm of PEDOT: PSS in place of MoO_x and did not have any ZnO NPs. The top electrode was 7 nm Ca/ 150 nm Al and was deposited by thermal evaporation with an area of 0.1 cm^2.

On the semi-transparent cells, Ag NWs were deposited by spray deposition from methanol at room temperature. Methanol was chosen to speed the evaporation of the spraying solvent compared to a higher boiling point solvent such as ethanol or isopropanol. The parameters of the spray deposition (see Supporting Information) were optimized over numerous trial runs to maximize transmission for a given sheet resistance. We found that it was important to perform our optimization using a substrate that resembled the surface of our semi-transparent cells as closely as possible. To this end, we performed our optimization by spraying Ag NWs on glass slides coated with ~25 nm of ZnO NPs.

Two more layers of ZnO NPs were then deposited on top of the Ag NWs by sequential spin coating steps. No annealing was performed during any part of the composite fabrication. The resulting Ag NW – ZnO

NP composite electrode had a total thickness of ~75 nm, as determined by SEM cross-section. Silver contacts to both the Ag NWs and the ITO were deposited by thermal evaporation to aid in electrical testing. Following deposition of the silver contact pads, extraneous active area was eliminated by scratching away all deposited layers (except the ITO). Combined with the pre-patterned ITO bottom electrode, this scratching step defined the active area (0.415 cm^2) of the semi-transparent devices. Finally, LiF was deposited as the top-most layer by thermal evaporation with a thickness of 90 nm.

Characterization: External quantum efficiency (EQE) spectra were measured inside the nitrogen glovebox using a halogen lamp for partial white light bias (~0.04 suns) to light soak the ZnO NPs. A monochromatic signal was chopped at 160 Hz and superimposed on top of the white light bias. Internal quantum efficiency was determined by dividing the measured EQE by the calculated absorption of the active layer. The absorption of the active layer was calculated by measuring the total transmission of the semi-transparent cell and subtracting from it the absorption and reflection of all the other layers in the device, as determined by transfer matrix modeling.[23–25]

Transmission measurements were made by placing devices directly in front of an integrating sphere to capture light transmitted both direct and diffusely through the entire device. Contributions to the optical losses were estimated from transfer matrix modeling, which is described in detail elsewhere.[23] The complex indices of refraction were measured independently by ellipsometry for all of the layers in the device except the Ag NWs. The optical loss of the Ag NWs was treated as a correction on the transfer matrix model, since Ag NWs do not give rise to coherent reflection in the way of the other thin films in the device stack. The correction was applied as the first layer in the device stack when light was incident on the Ag NW side of the device, and the last layer of the device stack when light was incident on the glass side. It was assumed that all of the Ag NW optical losses (1-transmission) were absorptive.

Hybrid tandem devices were fabricated in a mechanically stacked, 4-terminal configuration. CIGS cells were received from the National Renewable Energy Laboratory as completed devices including electrodes. The semi-transparent organic cell was stacked Ag NWs side up (glass side down) on top of the CIGS, such that their active areas were well-aligned. Lastly, a painted black optical mask was placed directly on top of the semi-transparent cell to define the illuminated areas of both subcells, and all layers were clamped together to fix them in place. The hybrid tandem efficiency was found by adding the maximum power outputs of the two subcells when measured in the stacked configuration, since in a 4-terminal configuration there are no current or voltage matching constraints. The efficiency of hybrid tandem photovoltaics was also calculated from the measured efficiency and transmission of the semi-transparent cells, and the known performance of the CIGS cell. The transmission of the semi-transparent cell was multiplied by the EQE spectrum of the CIGS cell and the photon flux of the AM 1.5 G spectrum and integrated to get the CIGS J_{sc}. Multiplying this calculated J_{sc} by the measured V_{oc} and *FF* of the CIGS cell when under a semi-transparent organic cell gave the efficiency of the CIGS subcell in the tandem configuration. It was assumed that the two cells were connected in a 4-terminal architecture so that their maximum powers could be added together to obtain the tandem efficiency.

Further details of the semi-transparent cell fabrication and characterization are given in the Supporting Information.

Supporting Information

Supporting Information is available from the Wiley Online Library or from the author.

Acknowledgements

This research was based upon work supported by the Department of Energy through the Bay Area Photovoltaic Consortium under Award Number DE-EE0004946, and by the Center for Advanced Molecular Photovoltaics (CAMP) (Award no. KUS-C1–015–21) made by the King Abdullah University of Science and Technology (KAUST). Work was performed in part at the Stanford Nanofabrication Facility's nSiL lab, which was funded by National Science Foundation (award ARI-0963061). Additional funding was provided by the National Defense Science and Engineering Graduate Fellowship (Z.M.B.), the National Science Foundation Graduate Research Fellowship (A.R.B.), Baseline Research Funding from KAUST (P.M.B.), and the TomKat Center for Sustainable Energy. Thanks to Rommel Noufi at the National Renewable Energy Laboratory for providing the CIGS cell used as the bottom cell of the hybrid tandem devices.

Received: May 2, 2013
Revised: July 1, 2013
Published online: October 7, 2013

[1] J. Krantz, T. Stubhan, M. Richter, S. Spallek, I. Litzov, G. J. Matt, E. Spiecker, C. J. Brabec, *Adv. Funct. Mater.* **2012**, *23*, 1711.
[2] C.-C. Chueh, S.-C. Chien, H.-L. Yip, J.-F. Salinas, C.-Z. Li, K.-S. Chen, F.-C. Chen, W.-C. Chen, A. K.-Y. Jen, *Adv. Energy Mater.* **2012**, *3*, 417.
[3] B. Norton, P. C. Eames, T. K. Mallick, M. J. Huang, S. J. McCormack, J. D. Mondol, Y. G. Yohanis, *Solar Energy* **2011**, *85*, 1629.
[4] J. A. Briggs, A. C. Atre, J. A. Dionne, *J. Appl. Phys.* **2013**, *113*, 124509.
[5] A. A. D. Adikaari, I. Etchart, P.-H. Guéring, M. Bérard, S. R. P. Silva, A. K. Cheetham, R. J. Curry, *J. Appl. Phys.* **2012**, *111*, 094502.
[6] Z. M. Beiley, M. D. McGehee, *Energ. Environ. Sci.* **2012**, *5*, 9173.
[7] M. W. Rowell, M. D. McGehee, *Energ. Environ. Sci.* **2010**, *4*, 131.
[8] J. A. Bartelt, Z. M. Beiley, E. T. Hoke, W. R. Mateker, J. D. Douglas, B. A. Collins, J. R. Tumbleston, K. R. Graham, A. Amassian, H. Ade, J. M. J. Fréchet, M. F. Toney, M. D. McGehee, *Adv. Energy Mater.* **2012**, *3*, 364.
[9] J. Hanisch, E. Ahlswede, M. Powalla, *Thin Solid Films* **2008**, *516*, 7241.
[10] S. Heum Park, B. Hoon Lee, J. Moon Shin, S.-Y. Jeong, S. Song, H. Suh, K. Lee, *Appl. Phys. Lett.* **2012**, *100*, 133306.
[11] H. P. Kim, H. J. Lee, A. R. B. Mohd Yusoff, J. Jang, *Sol. Energ. Mat. Sol. C.* **2013**, *108*, 38.
[12] J. Czolk, A. Puetz, D. Kutsarov, M. Reinhard, U. Lemmer, A. Colsmann, *Adv. Energy Mater.* **2012**, *3*, 386.
[13] Z. Tang, Z. George, Z. Ma, J. Bergqvist, K. Tvingstedt, K. Vandewal, E. Wang, L. M. Andersson, M. R. Andersson, F. Zhang, O. Inganäs, *Adv. Energy Mater.* **2012**, *2*, 1467.
[14] Y. Zhou, H. Cheun, S. Choi, C. Fuentes-Hernandez, B. Kippelen, *Org. Electron.* **2011**, *12*, 827.
[15] K.-S. Chen, J.-F. Salinas, H.-L. Yip, L. Huo, J. Hou, A. K.-Y. Jen, *Energ. Environ. Sci.* **2012**, *5*, 9551.
[16] Y. H. Kim, L. Müller-Meskamp, A. A. Zakhidov, C. Sachse, J. Meiss, J. Bikova, A. Cook, A. A. Zakhidov, K. Leo, *Sol. Energ. Mat. Sol. C.* **2012**, *96*, 244.
[17] H. Park, S. Chang, M. Smith, S. Grade ak, J. Kong, *Sci. Rep.* **2013**, *3*, doi: 10.1038/srep01581.
[18] E. C. Garnett, W. Cai, J. J. Cha, F. Mahmood, S. T. Connor, M. G. Christoforo, Y. Cui, M. D. McGehee, M. L. Brongersma, *Nat. Mater.* **2012**, *11*, 241.
[19] J.-Y. Lee, S. T. Connor, Y. Cui, P. Peumans, *Nano Lett.* **2010**, *10*, 1276.
[20] F. Guo, X. Zhu, K. Forberich, J. Krantz, T. Stubhan, M. Salinas, M. Halik, S. Spallek, B. Butz, E. Spiecker, T. Ameri, N. Li, P. Kubis, D. M. Guldi, G. J. Matt, C. J. Brabec, *Adv. Energy Mater.* **2013**, doi: 10.1002/aenm.201300100.
[21] C.-C. Chen, L. Dou, R. Zhu, C.-H. Chung, T.-B. Song, Y. B. Zheng, S. Hawks, G. Li, P. S. Weiss, Y. Yang, *ACS Nano* **2012**, *6*, 7185.

[22] M. Reinhard, R. Eckstein, A. Slobodskyy, U. Lemmer, A. Colsmann, *Org. Electron.* **2012**, *14*, 273.
[23] G. F. Burkhard, E. T. Hoke, M. D. McGehee, *Adv. Mater.* **2010**, *22*, 3293.
[24] L. A. A. Pettersson, L. S. Roman, O. Inganäs, *J. Appl. Phys.* **1999**, *86*, 487.
[25] P. Peumans, A. Yakimov, S. R. Forrest, *J. Appl. Phys.* **2003**, *93*, 3693.
[26] J. Krantz, M. Richter, S. Spallek, E. Spiecker, C. J. Brabec, *Adv. Funct. Mater.* **2011**, *21*, 4784.
[27] W. Gaynor, J.-Y. Lee, P. Peumans, *ACS Nano* **2010**, *4*, 30.
[28] W. Gaynor, G. F. Burkhard, M. D. McGehee, P. Peumans, *Adv. Mater.* **2011**, *23*, 2905.
[29] J.-Y. Lee, S. T. Connor, Y. Cui, P. Peumans, *Nano Letters* **2008**, *8*, 689.
[30] C.-H. Chung, T.-B. Song, B. Bob, R. Zhu, H.-S. Duan, Y. Yang, *Adv. Mater.* **2012**, *24*, 5499.
[31] Z. Yu, L. Li, Q. Zhang, W. Hu, Q. Pei, *Adv. Mater.* **2011**, *23*, 4453.
[32] D.-S. Leem, A. Edwards, M. Faist, J. Nelson, D. D. C. Bradley, J. C. de Mello, *Adv. Mater.* **2011**, *23*, 4371.
[33] F. S. F. Morgenstern, D. Kabra, S. Massip, T. J. K. Brenner, P. E. Lyons, J. N. Coleman, R. H. Friend, *Appl. Phys. Lett.* **2011**, *99*, 183307.
[34] J. Ajuria, I. Ugarte, W. Cambarau, I. Etxebarria, R. Tena-Zaera, R. Pacios, *Sol. Energ. Mat. Sol. C.* **2012**, *102*, 148.
[35] T. Stubhan, J. Krantz, N. Li, F. Guo, I. Litzov, M. Steidl, M. Richter, G. J. Matt, C. J. Brabec, *Sol. Energ. Mat. Sol. C.* **2012**, *107*, 248.
[36] S. Mehra, M. G. Christoforo, P. Peumans, A. Salleo, *Nanoscale* **2013**, doi: 10.1039/c3nr00863k.
[37] C. Pacholski, A. Kornowski, H. Weller, *Angew. Chem. Int. Ed.* **2002**, *41*, 1188.
[38] P. Sharma, K. Sreenivas, K. V. Rao, *J. Appl. Phys.* **2003**, *93*, 3963.
[39] S. Nam, H. W. Cho, S. Lim, D. Kim, H. Kim, B. J. Sung, *ACS Nano* **2013**, *7*, 851.
[40] T. Kim, Y. W. Kim, H. S. Lee, H. Kim, W. S. Yang, K. S. Suh, *Adv. Funct. Mater.* **2012**, *23*, 1250.
[41] Y. Sun, G. C. Welch, W. L. Leong, C. J. Takacs, G. C. Bazan, A. J. Heeger, *Nat. Mater.* **2011**, *11*, 44.
[42] J. J. Jasieniak, J. Seifter, J. Jo, T. Mates, A. J. Heeger, *Adv. Funct. Mater.* **2012**, *22*, 2594.
[43] C. Cabanetos, A. El Labban, J. A. Bartelt, J. D. Douglas, W. R. Mateker, J. M. J. Fréchet, M. D. McGehee, P. M. Beaujuge, *J. Am. Chem. Soc* **2013**, *135*, 4656.
[44] J. D. Kotlarski, P. W. M. Blom, *Appl. Phys. Lett.* **2012**, *100*, 013306.
[45] Z. M. Beiley, E. T. Hoke, R. Noriega, J. Dacuna, G. F. Burkhard, J. A. Bartelt, A. Salleo, M. F. Toney, M. D. McGehee, *Adv. Energy Mater.* **2011**, *1*, 954.
[46] M. A. Faist, T. Kirchartz, W. Gong, R. S. Ashraf, I. McCulloch, J. C. de Mello, N. J. Ekins-Daukes, D. D. C. Bradley, J. Nelson, *J. Am. Chem. Soc* **2012**, *134*, 685.
[47] J. H. Seo, D.-H. Kim, S.-H. Kwon, M. Song, M.-S. Choi, S. Y. Ryu, H. W. Lee, Y. C. Park, J.-D. Kwon, K.-S. Nam, Y. Jeong, J.-W. Kang, C. S. Kim, *Adv. Mater.* **2012**, *24*, 4523.
[48] T. Kim, J. Y. Choi, J. H. Jeon, Y.-S. Kim, B.-S. Kim, D.-K. Lee, H. Kim, S. Han, K. Kim, *Mater. Res. Bull.* **2012**, *47*, 3040.
[49] J. You, L. Dou, K. Yoshimura, T. Kato, K. Ohya, T. Moriarty, K. Emery, C.-C. Chen, J. Gao, G. Li, Y. Yang, *Nat. Commun.* **2013**, *4*, 1446.
[50] Y. Galagan, D. J. D. Moet, D. C. Hermes, P. W. M. Blom, R. Andriessen, *Org. Electron.* **2012**, *13*, 3310.
[51] D. Gupta, M. M. Wienk, R. A. J. Janssen, *Adv. Energy Mater.* **2013**, doi: 10.1002/aenm.201201061.